X-ray spectroscopic investigation of crystal fields in $Ce_2Rh_{1-x}Ir_xIn_8$ heavy fermions

D. S. Christovam,[1] A. Marino,[1] J. Falke,[1] C.-E. Liu,[2] C.-F. Chang,[1] C.-Y. Kuo,[2,3] O. Stockert,[1] S. Wirth,[1] M. W. Haverkort,[4] G. Zwicknagl,[5,1] A. Severing,[6,1] P. F. S. Rosa,[7] A. M. Caffer,[8] M. H. Carvalho,[7,8] and P. G. Pagliuso[8]

[1]*Max Planck Institute for Chemical Physics of Solids, Nöthnitzer Str. 40, 01187 Dresden, Germany*
[2]*Department of Electrophysics, National Yang Ming Chiao Tung University, Hsinchu 30010, Taiwan*
[3]*National Synchrotron Radiation Research Center, 101 Hsin-Ann Road, 30076 Hsinchu, Taiwan*
[4]*Institute for Theoretical Physics, Heidelberg University, Philosophenweg 19, 69120 Heidelberg, Germany*
[5]*Institut für Mathematische Physik, Technische Universität Braunschweig, Mendelssohnstraße 3, 38106 Braunschweig, Germany*
[6]*Institute of Physics II, University of Cologne, Zülpicher Str. 77, 50937 Cologne, Germany*
[7]*Los Alamos National Laboratory, Los Alamos, New Mexico 87545, USA*
[8]*Instituto de Física "Gleb Wataghin", UNICAMP, 13083-970 Campinas-SP, Brazil*

(Received 13 June 2024; revised 13 August 2024; accepted 14 August 2024; published 29 August 2024)

The higher dimensionality in the crystal fields of the Ce_2MIn_8 (M = Rh, Ir) compounds and its interplay with hybridization and disorder are key ingredients to understand the complex phase diagrams by this family, which have been explored extensively by macroscopic techniques. Here, we present an investigation of the crystal-electric field schemes of $Ce_2Rh_{1-x}Ir_xIn_8$ using x-ray absorption spectroscopy. Our full multiplet calculations for the $4f^1$ configuration of Ce^{3+} to describe the temperature-dependent linear dichroism in Ce_2MIn_8 are consistent with a $\Gamma_7^1 = \sqrt{1-\alpha^2}\cdot|\mp\frac{3}{2}\rangle - |\alpha|\cdot|\pm\frac{5}{2}\rangle$ ground state containing a predominant $|\pm 3/2\rangle$ contribution that increases further with x. This enhancement is believed to favor superconductivity in Ce-based heavy fermion materials, observed in previous results in the $CeMIn_5$ family. Our recent observations shed light on the unexpected emergence of the ambient-pressure superconducting dome in the center of the composition phase diagram and its subsequent suppression on the Ir-rich side due to the early onset of fluctuations associated with the structurally more disordered state, inferred from previous neutron magnetic diffraction experiments.

DOI: 10.1103/PhysRevB.110.075161

I. INTRODUCTION

Ce-based intermetallic compounds exhibit a plethora of unusual states at low temperatures including heavy Fermi liquids, unconventional superconductivity, and complex magnetism [1]. The ground states are separated by quantum critical points through which the systems can be tuned by applying magnetic fields and pressure or by substituting non-f elements. The key to understanding the complex phase diagrams are local dynamics of the strongly correlated Ce $4f$ electrons and their coupling to the weakly correlated conduction electrons. The latter removes the magnetic degeneracy of the partially filled $4f$ shells by inducing long-range magnetic orders or by forming (local) Kondo singlets via the Kondo effect [2–5].

As such, our focus is in the evolution of the local $4f$ dynamics resulting from isoelectronic substitutions of non-f metal ions. Of particular importance is the orbital anisotropy of the Ce $4f$ ground state wave function. The systematic study of benchmark heavy fermion compounds $CeRh_{1-x}Ir_xIn_5$ and $CeCoIn_5$ [6–10] demonstrated that the shape of the Ce $4f$ wave function serves as a good predictor of whether a given material becomes magnetic or develops heavy fermion superconductivity (SC). It had already been suggested that a lower structural dimensionality could be reflected into electronic properties favoring superconducting ground states [11], and the observation of stronger out-of-plane character of the ground state wavefunction correlates nicely with the emergence of SC at higher superconducting critical temperatures (T_c). Conversely, a flatter orbital distribution appears to favor magnetic states [10].

Following up this track of thought we investigate the anisotropy of the $4f$ wave function in the series $Ce_2Rh_{1-x}Ir_xIn_8$. The high tunability of ground state properties of the Ce_mMIn_{3m+2} (M = Co, Rh, Ir; m = 1, 2) allows for displays of unconventional SC, occasionally coexisting with complex magnetism. Such intricate phase diagrams are a result of the interplay between crystalline-electric field effects (CEF), Ruderman-Kittel-Kasuya-Yosida (RKKY) interaction and the Kondo effect. From its cubic counterpart, $CeIn_3$, to the more 2D members of this tetragonal family, $CeMIn_5$ (m = 1; Ce115), the different crystalline environments tuning the ground state properties toward SC have been explored [12]. Including the more tridimensional Ce_2MIn_8 (m = 2; Ce218) to the series, it constitutes the perfect playground to explore

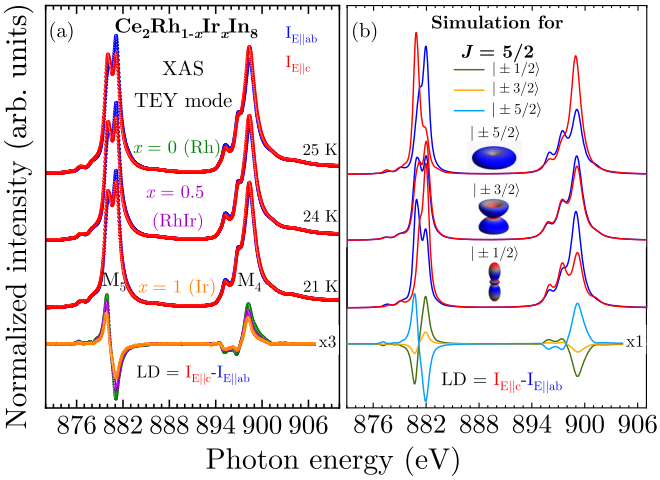

FIG. 1. (a) From top, linear polarized XAS (TEY) spectra of Ce_2RhIn_8, $Ce_2Rh_{0.5}Ir_{0.5}In_8$, and Ce_2IrIn_8 at about 25 K for $\vec{E} \parallel c$ (red) and $\vec{E} \parallel ab$ plane (blue), and respective linear dichroism (green, purple, and orange) at the bottom. (b) Calculated linearly polarized spectra, corresponding charge densities, and resulting dichroisms (bottom) for pure $|\pm J_z\rangle$ states.

the role of structural dimensionality itself as a tuning parameter, and gather information on how effective the CEF ground state wavefunction is as indicative of SC in a broader space of Ce-based compounds.

In the Ce115 system, the Ce^{3+} Hund's rule ground state is split into three Kramer's doublets, namely,

$$\Gamma_7^1 : \left\{ \sqrt{1-\alpha^2} \left| \pm\frac{3}{2} \right\rangle - |\alpha| \left| \mp\frac{5}{2} \right\rangle \right\}, \quad (1)$$

$$\Gamma_7^2 : \left\{ |\alpha| \left| \mp\frac{3}{2} \right\rangle + \sqrt{1-\alpha^2} \left| \pm\frac{5}{2} \right\rangle \right\}, \quad (2)$$

$$\Gamma_6 : \left\{ \left| \pm\frac{1}{2} \right\rangle \right\}, \quad (3)$$

for it is located in a D_{4h}-symmetric site. In particular, the CEF investigation of $CeCoIn_5$ and the $CeRh_{1-x}Ir_xIn_5$ substitution series showed the ground state wave functions that are predominantly $|\pm 5/2\rangle$, the state with the donut shaped charge density [see Fig. 1(b)], seemingly favors magnetism, while the Ising-like $|\pm 3/2\rangle$-rich state [*yo-yo* shaped; see Fig. 1(b)] favors superconductivity [10]. This large out-of-plane to in-plane density ratio might be understood as a reflection of the lower dimensionality in these compounds with respect to $CeIn_3$ since they consist of blocks of the latter intercalated by MIn_2 layers [13]. Indeed, also the Fermi surface of these materials is known to be quasi 2D [14–18].

In contrast, the Ce218 compounds are less explored. This family displays an equally fascinating phase diagram as the prominent Ce115 family, exhibiting two superconducting domes with strikingly different pressure evolution, coexistence with antiferromagnetism, and emergence of a spin-freezing phase on the Ir-rich side of the Rh-Ir diagram [19–22]. For M = Rh, a SC dome emerges as applied pressure suppresses magnetic order in the vicinity of quantum criticality, in a similar fashion to $CeRhIn_5$. As Ir concentration increases, another SC region appears on the phase diagram, however, it is quickly suppressed upon pressurizing the system. We note that their T_c are lower than in their Ce115 counterparts, and the Néel temperatures, T_N, are higher. Furthermore, the structural disorder is more pronounced than in the Ce115, showing stacking faults and intralayer In inclusions [13,23–25]. The Ce218 family has a second $CeIn_3$ block between the MIn_2 layers, leading to a breaking of a mirror plane at the Ce site. As a result, the Ce point symmetry becomes C_{4v}. The CEF potential is still well described by D_{4h} (same terms surviving in the CEF potential expansion) [26] so that a comparison between $CeIn_3$, Ce218, and Ce115 is still viable.

The CEF in the Ce218 family has so far only been investigated with macroscopic measurements, e.g., the high-temperature magnetic anisotropy has been analyzed in terms of a crystal-field split Hund's rule ground state [27,28]. Spectroscopy data are not available to date. X-ray absorption spectroscopy (XAS) at the Ce $M_{4,5}$ edges ($3d^{10}4f^1 \rightarrow 3d^94f^2$) is the ideal tool to probe the CEF ground state wave function and find out whether the ground state has $|\Gamma_6\rangle = |\pm 1/2\rangle$ or $|\Gamma_7\rangle$ (combination of states with $m_z \pm 3/2$ and $\mp 5/2$) symmetry, and in case of the latter, to determine the mixing factor α. The technique exploits dipole selection rules of linear polarized light: each $|J_z\rangle$ state has its own characteristic linear dichroism (LD) (see Fig. 1(b) [29,30]). At low temperatures, only the ground state is probed. As temperature is increased, excited CEF states become occupied, the superposition of signals provides insight into the sequence of CEF states and splitting energies $\Delta_{1,2}$. We do note that the sign of the $|\Gamma_7\rangle$ state cannot be determined with a dipole method like XAS [31]. For this reason we shall not define this sign but will use indexes 1 and 2 to refer to their energies.

We report temperature-dependent XAS measurements in single crystals of $Ce_2Rh_{1-x}Ir_xIn_8$ ($x = 0, 0.5, 1$). Making use of full multiplet calculations, we are able to answer questions posed previously regarding the CEF evolution with Ir content, understand the emergence of the ambient-pressure superconducting dome, and the role of Kondo hybridization and disorder in defining the Ce218 phase diagram.

II. EXPERIMENT AND ANALYSIS

Single-crystalline samples of $Ce_2Rh_{1-x}Ir_xIn_8$ ($x = 0$, 0.5, 1) were grown by the self-flux method [11,32,33] and screened macroscopically through magnetization measurements in a commercial superconducting quantum interference device (SQUID)-vibrating-sample magnetometer (VSM). The morphology of the crystals was well defined, namely plates stacked with the [001] direction normal to their plane.

XAS at the Ce $M_{4,5}$ edges (880–904 eV) was performed at the NSRRC-MPI Submicron soft x-ray spectroscopy beamline TPS45A1 [34] at the Taiwan Photon Source. The overall energy resolution was 70 meV. The crystals were aligned using the Laue method and mounted such that a surface with a [100] normal vector was exposed to the beam. As such, both polarizations, $\vec{E} \parallel ab$ and $\vec{E} \parallel c$, could be measured simultaneously without rotating the sample. The mounted crystals were cleaved *in situ* using a knife-anvil setup to expose a clean surface in an ultrahigh vacuum of the order of 2.5×10^{-10} mbar prior to inserting them into the main chamber

with a base pressure of $1.0-1.8\times10^{-10}$ mbar. The spectra were acquired in the total-electron-yield (TEY) mode by measuring the sample drain current at normal incidence geometry. XAS data were taken upon cooling down from 310 to 210, 150, 100, 60, and 25 K.

The data were analyzed with the full multiplet code *Quanty* [35]. The starting parameters come from the Cowan code [36], and typical reductions for the respective Hartree-Fock values of the $4f$-$4f$ and $3d$-$4f$ Slater integrals, and $3d$ spin-orbit values are applied to best reproduce the isotropic spectra, $I_{\rm iso} = (2\,{\rm I}_{\parallel ab} + {\rm I}_{\parallel c})/3$ [29]. The reductions account for configuration interaction effects that are not considered in the Hartree-Fock scheme [37]. Furthermore, a Gaussian and a Lorentzian broadening are applied to account for resolution and lifetime effects, respectively. After setting these reduction factors, the CEF parameters are iteratively adjusted to reproduce the LD that arises from the impact of CEF effects. For D_{4h} symmetry, these parameters can be expressed in terms of the energies of the excited states relative to the ground state, Δ_1, Δ_2, and the J_z mixing coefficient α as the contribution of $|\pm5/2\rangle$ in the $|\Gamma_7^1\rangle = \sqrt{1-\alpha^2}\cdot|\mp\frac{3}{2}\rangle - |\alpha|\cdot|\pm\frac{5}{2}\rangle$ state.

III. RESULTS AND DISCUSSION

Figure 1(a) presents the polarization-dependent XAS data of Ce_2RhIn_8, $Ce_2Rh_{0.5}Ir_{0.5}In_8$, and Ce_2IrIn_8 at roughly 25 K (red and blue circles), with the experimental linear dichroism shown at the bottom as $\mathrm{LD} = \mathrm{I}_{E||c} - \mathrm{I}_{E||ab}$ (green, purple, and orange circles).

The LD of all three compositions has the same sign, but their overall magnitude decreases as the Ir content increases. Panel (b) of Fig. 1 displays full multiplet simulations for the pure $|J_z\rangle$ states. Assuming that at 25 K the LD originates solely from the anisotropic charge density of the ground state (see below), a comparison of data and simulations reveals that the $|\Gamma_6\rangle$ ($|\pm1/2\rangle$) state can be immediately excluded as the ground state for all three compounds, because its LD sign does not match the experimental data in panel 1(a). This is consistent with previous macroscopic reports [27,28,38,39]. We see that the sign of LD at this temperature resembles best the pure $|\pm5/2\rangle$. This points toward a $|\Gamma_7\rangle$ (mixture of $|\pm3/2\rangle$ and $|\mp5/2\rangle$), with α decreasing with Ir content. It is important to note that the pure $|\pm5/2\rangle$ LD is much stronger than that of the pure $|\pm3/2\rangle$, so that even a balanced admixture richer in $|\pm3/2\rangle$ contribution would display the sign of the $|\pm5/2\rangle$ lineshape, as the spectral weights contribute with α^2 [compare LD in Fig. 1(a) and 1(b)]. To avoid confusion, the ground state is parametrized as $|\Gamma_7^1\rangle = \sqrt{1-\alpha^2}\cdot|\pm3/2\rangle - |\alpha|\cdot|\mp5/2\rangle$.

Before analyzing the low T XAS data quantitatively, we turn to the LD's temperature dependence for the Ce M_5 edge [see Figs. 2(a)–2(c)]. For Ce_2RhIn_8 and $Ce_2Rh_{0.5}Ir_{0.5}In_8$, the LD increases slightly when warming from 25 to 60 K, and it increases up to 100 K for Ce_2IrIn_8, before decreasing with further rising temperature [see insets of Figs. 2(a) and 2(c)]. Here it is again useful to refer to the pure $|\pm J_z\rangle$ states in Fig. 1(b). We can reason that the nonabrupt increase of LD(T) must be a consequence of the ground state being a mixed $|\Gamma_7\rangle$ state with a significant amount of $|\pm3/2\rangle$, the first excited state being the other $|\Gamma_7^2\rangle = |\alpha|\cdot|\mp\frac{3}{2}\rangle + \sqrt{1-\alpha^2}\cdot|\pm\frac{5}{2}\rangle$ state of

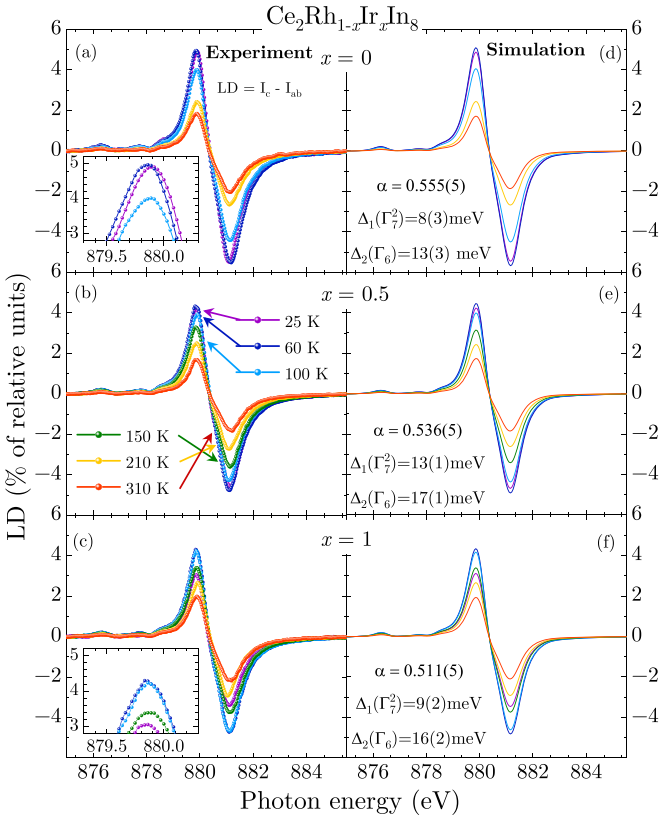

FIG. 2. (left) Experimental T dependence of the LD at $T = 25$ (purple), 60 (blue), 100 (light blue), 150 (green), 210 (yellow), and 310 K (red) for (a) Ce_2RhIn_8, (b) $Ce_2Rh_{0.5}Ir_{0.5}In_8$, and (c) Ce_2IrIn_8. The insets zoom in to the maximum of the dichroic signal. (right) (d), (e) Respective CEF full multiple simulations. The excited states are populated according to Boltzmann statistics. The scale was multiplied by 100 to show the percentage of LD.

majority $|\pm5/2\rangle$, leaving the $|\Gamma_6\rangle = |\pm1/2\rangle$ to compensate the LD as second excited state.

For the quantitative analysis, we construct the isotropic XAS spectrum for each sample from the linearly polarized data set, shown in Fig. 3, and simulate the data as described above. The black curves demonstrate the excellent agreement with the full multiplet ionic model of a $4f^1$ configuration without considering the CEF yet [the $4f$-$4f$ and $3d$-$4f$ Slater integrals, and the atomic value for the $3d$ spin orbit were reduced on average by 32.90(1)%, 19.5(1)%, and 2.78(1)%, respectively]. Neither the postedge continuum, nor the minute satellites (see blue arrows) on the tail of the main $M_{4,5}$ absorption edges are considered in our calculations. The latter are due to the transition $3d^{10}4f^0 \rightarrow 3d^94f^1$, indicating the presence of the Kondo effect (see the inset of Fig. 3). We recall that as hybridization of $4f$ and conduction electrons sets in, the ground state becomes a quantum mechanically mixed state of Ce^{3+} ($4f^1$) and Ce^{4+} ($4f^0$). The XAS process creates a core hole that acts differently with the tri- and tetravalent states, leading to a split in energy in the final states. As a result, a satellite peak, arising from the $4f^0$ contribution in the mixed ground state, appears in the spectra [40,41]. Thus, in this context, it is not uncommon to attribute the origin of

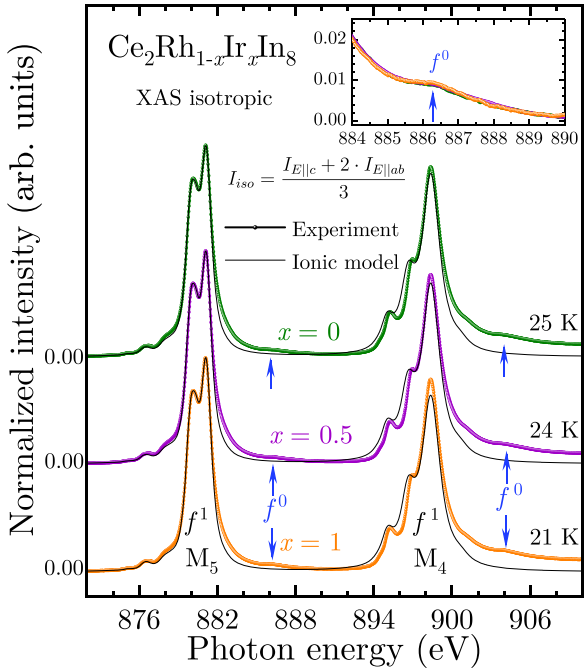

FIG. 3. Low-T isotropic XAS spectrum of $Ce_2Rh_{1-x}Ir_xIn_8$ ($x = 0, 0.5, 1$) (dots) and the corresponding ionic multiplet calculation (solid line). Blue arrows point out satellites due to f^0 in the initial state. Inset: f^0 satellites at M_5 edge of all three compounds (blue arrows) on an expanded scale.

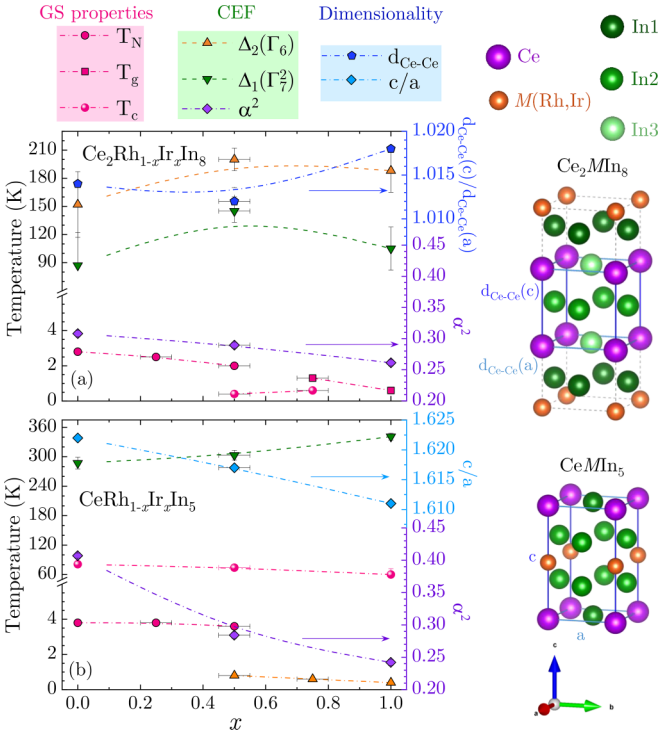

FIG. 4. Summary of physical properties of (a) Ce_2MIn_8 and (b) $CeMIn_5$ along with respective structures, with the Ce-Ce crystallographic distances highlighted. The closed circles represent T_N, open circles refer to T_c and squares to the freezing temperature T_g. Triangles mark the energy splittings $\Delta_1(\Gamma_7^2)$ of $|\pm 5/2\rangle$ rich $|\Gamma_7^2\rangle = |\alpha| \cdot |\mp\frac{3}{2}\rangle + \sqrt{1-\alpha^2} \cdot |\pm\frac{5}{2}\rangle$ (down), $\Delta_2(\Gamma_6)$ - $|\pm\frac{1}{2}\rangle$ doublet (up), and α^2 is represented by diamonds (bottom-right side scale). Finally, the dimensionality parameters $d_{Ce-Ce}(c)/d_{Ce-Ce}(a)$ and c/a are also shown with respective scales on the top-right side. Crystallographic parameters and transition temperatures of the Ce218 extracted from [25,28] and all data regarding Ce115 adapted from [9–11,13].

hybridization with the singlet $4f^0$ state to Kondo interaction [42].

Having achieved the modeling of the isotropic spectra, we now turn to the CEF analysis of the temperature dependent LD in Figs. 2(a)–2(c). Starting from the previous CEF models proposed from thermal expansion, magnetic anisotropy, and specific heat measurements [27,28,39], we modify Δ_1, Δ_2, and α for each compound in order to get the best possible description at all temperatures [some considerations on fit quality are provided in the Appendix]. We find CEF models that provide very good agreement with the T dependent LDs and simulations for all three compounds [see Figs. 2(d)–2(f)]. The respective mixing factors for the $|\Gamma_7\rangle$ ground state and the CEF transition energies are listed. We find the planar admixture of $|\pm 5/2\rangle$ is indeed the minor spectral contribution in the ground state, $\alpha^2 \approx 0.25$, for all three compounds, so that all three ground state charge densities are more extended along c than in the ab plane. Furthermore, the $|\pm 5/2\rangle$ and $|\mp 3/2\rangle$ admixture is changing only minimally within the series, the $|\pm 5/2\rangle$ contribution being smallest in the Ir compound.

The inset of Fig. 3 illustrates that the f^0 contributions in the initial states are small and identical for all three compounds within our energy resolution and experimental uncertainty of 0.04% of relative LD intensity (maximum variance observed), suggesting the Kondo effect plays only a minor role and does not increase when replacing Rh by Ir. The subordinate role of the Kondo effect justifies the Boltzmann analysis of the T-dependent data. To verify further the CEF parameters are consistent with macroscopic measurements, we compare our results of Ce_2RhIn_8 to literature values. Thermal expansion reveals excited states at 6.1(5) and 16.8(9) meV, respectively, which align well with our scheme. Similarly, we find comparable values for the B_2^0 crystal-field parameter derived from the anisotropic Curie-Weiss temperatures θ_{ab} and θ_c, using $B_2^0 = 10/3 \cdot (\theta_{ab} - \theta_c)/(2J-1)(2J+3)$ with $J = 5/2$ [43], and from our XAS analysis. The inverse susceptibilities obtained by Bao *et al.* [44] suggest $B_2^0 \approx -5.4$ K, while our XAS analysis yields $B_2^0 \sim -5.9$ K. Therefore, we are confident to have captured the CEF splittings correctly.

Figure 4 summarizes the crystal-field mixing factors and transition energies from the XAS analysis for the $Ce_2Rh_{1-x}Ir_xIn_8$ (b) and $CeRh_{1-x}Ir_xIn_5$ (c) families. We also include physical quantities such as T_c, T_N and a spin-freezing temperature T_g, as well as dimensionality parameters such as the ratio of the tetragonal lattice constants a and c (relevant for Ce115) or the ratio of the Ce-Ce distances along a and c denoted as $d_{Ce-Ce}(c)/d_{Ce-Ce}(a)$ (equivalent parameter for Ce218).

The contribution from $|\pm 5/2\rangle$ decreases with the introduction of Ir into the system, mirroring the behavior in the Ce115 compounds ($\alpha_{Rh}^2 = 0.407$ to $\alpha_{Ir}^2 = 0.242$) [10,31]. However, for the Ce218, this effect is more modest: the

reduction in α^2 from Rh to Ir is of 4.7% in the Ce218s in comparison to 16.5% in the Ce115s. As proposed in [28], α^2_{Ce218} is in average also closer to the cubic admixing of $CeIn_3$, wherein $\alpha^2 = 1/6 \approx 0.167$ [45]. The single-ion anisotropy determines the ground state's magnetic moment, and a cubiclike charge distribution allows for the out-of-plane moment aligned observed in neutron magnetic diffraction. It also suggests, similar to the more two dimensional Ce115 compounds, that increasing the contribution of $|\mp 3/2\rangle$ in the ground state could enhance superconductivity, and indeed, $Ce_2Rh_{0.5}Ir_{0.5}In_8$ exhibits superconductivity at ambient pressure [19], albeit with a lower T_c compared to $CeRh_{0.5}Ir_{0.5}In_5$ [46], attributed to its increased dimensionality [compare the ground state properties and α^2 evolution with x in Figs. 4(b) and 4(c)].

The splitting energies in the Ce218 system do not seem to behave monotonically. $\Delta_1(\Gamma_7^2)$ of the $|\pm 5/2\rangle$ rich $|\Gamma_7^2\rangle = |\alpha| \cdot |\mp\frac{3}{2}\rangle + \sqrt{1-\alpha^2} \cdot |\pm\frac{5}{2}\rangle$ and $\Delta_2(\Gamma_6)$ of the $|\pm\frac{1}{2}\rangle$ doublet are largest for the $x = 0.5$ sample. This rules out the speculative scheme proposed in [28] regarding the CEF scheme of Ce_2IrIn_8. We would like to point out that the maximum in the CEF splittings in $Ce_2Rh_{0.5}Ir_{0.5}In_8$ coincides with a dip in the ratio of Ce-Ce distances, i.e., the splittings are largest for the most compressed Ce cage in the $Ce_2Rh_{1-x}Ir_xIn_8$ series [see structure in Fig. 4(a)].

New questions arise, particularly regarding the high-temperature maximum at ~50 K in Ce_2IrIn_8's resistivity, which contrasts with the maximum in Ce_2RhIn_8, one order of magnitude lower. Additionally, the suppression of superconductivity on the Ir-rich side of the series [47] demands attention. We argue that the common factor linking these questions is the onset of disorder in the form of a spin-glass phase. A resistivity maximum in a Kondo lattice typically indicates the crossover from incoherent to coherent scattering, which can provide an estimate of the energy scales involved as, e.g., in $CeCoIn_5$ [48]. However, in $Ce_2Rh_{1-x}Ir_xIn_8$ the LD's T dependence aligns well with Boltzmann statistics, unlike systems where the Kondo and CEF energy scales are more comparable [26]. Furthermore, macroscopic experiments such as the unchanged effective moment observed in the magnetic susceptibilities with Ir concentration [27,28] suggest that the increase of the Kondo effect may not be as significant as one would expect if the resistivity maximum was purely due to Kondo coherence. The observation that the CEF schemes have comparable strength in all three compounds, combined with the likelihood that the Kondo effect does not increase dramatically as it does, e.g., from $CeRhIn_5$ to $CeIrIn_5$, where the effective and ordered moments are much more screened [48], further supports this view. The significant increase in the resistivity maximum already at $x = 0.5$ where structural disorder is expected to be most pronounced, strongly suggests that disorder, rather than coherence alone, plays a crucial role. In fact, in a quasi-2D system, such disorder could significantly contribute to the resistivity upturn at lower temperatures, similar to the behavior observed in UPt_2Si_2 [49]. Moreover, we speculate that the short-range interactions associated with this disorder may occur with much smaller Ir content than the actual composition initially manifesting as T_g. This hypothesis is supported by neutron magnetic diffraction studies conducted in $Ce_2Rh_{0.5}Ir_{0.5}In_8$ previously [28], where the order parameter exhibits an almost linear behavior, suggestive of fluctuations competing with the anticipated mean-field behavior for a simple antiferromagnetic phase. If such fluctuations could indeed emerge in this region of the phase diagram, it would not be surprising to observe the rapid suppression of superconductivity.

IV. CONCLUSIONS

XAS experiments provide the first spectroscopic determination of the crystal-field schemes of Ir-substituted Ce_2RhIn_8. Increasing the Ir content increases the out-of-plane $|\pm 3/2\rangle$ component in the $|\pm 3/2\rangle$ and $|\pm 5/2\rangle$ admixed $|\Gamma_7\rangle$ ground state, which is expected to favor the emergence of superconductivity, following the example of the Ce115 Rh/Ir substitution series. XAS data further show that the f^0 contribution in the ground state does not increase from Ce_2RhIn_8 to Ce_2IrIn_8, suggesting the Kondo effect plays a minor role in the physical properties upon substitution. We argue that the suppression of superconductivity on the Ir rich side is due to fluctuations arising from spin disorder in the spin-glass phase.

ACKNOWLEDGMENTS

All authors thank Manuel Brando, Otavio L. Canton, Miguel F. Carvalho, Eduardo Granado, and Daisuke Takegami for enlightening discussions. A.S. benefited from support of the German Research Foundation (DFG), Project No. 387555779. G.Z. acknowledges that this research was supported in part by Grant No. NSF PHY-2309135 to the Kavli Institute for Theoretical Physics (KITP). A.M.C., M.H.C., and P.G.P. benefited from support from Fundação de Amparo à Pesquisa do Estado de São Paulo (FAPESP) (São Paulo, Brazil; Grants No. 20/10580-8 and No. 22/16823-5), Conselho Nacional de Desenvolvimento Científico e Tecnológico (CNPq) (Brazil, Grants No. 405408/2023-4714 and No. 311783/2021-0), and Coordenação de Aperfeiçoamento de Pessoal de Nível Superior (CAPES) (Brazil). Work at Los Alamos was performed under the auspices of the U.S. Department of Energy, Office of Science, Basic Energy Sciences, Materials Sciences and Engineering Division. We acknowledge support from the Max Planck-POSTECH-Hsinchu Center for Complex Phase Materials.

APPENDIX A: CRYSTAL FIELD PARAMETERS

The full multiplet calculations performed in *Quanty* consist in solving iteratively the system's Hamiltonian $\mathcal{H} = \mathcal{H}_0 + \mathcal{H}_{SOC} + \mathcal{H}_{e-e} + \mathcal{H}_{CEF}$, where $\mathcal{H}_0$ describes the kinetic energy of the electrons and their attraction to the nucleus, $\mathcal{H}_{SOC}$ is the

TABLE I. Crystal field parameters (in meV) obtained from XAS analysis, corresponding to the schemes in Fig. 2.

x	A_2^0	A_4^0	A_4^4/A_4^{-4}
0	12.1(1)	36.4(1)	−19.5(1)
0.5	11.9(1)	48.4(1)	−31.9(1)
1	14.2(1)	47.7(1)	−22.5(1)

spin-orbit coupling, $\mathcal{H}_{e-e}$ is the full electron-electron term, and the tetragonal crystal field term $\mathcal{H}_{CEF}$ is expressed as a function of the usual A_k^m parameters:

$$\mathcal{H}_{CEF} = A_2^0\hat{C}_2^0 + A_4^0\hat{C}_4^0 + A_4^4\hat{C}_4^4 + A_4^{-4}\hat{C}_4^{-4}.$$

Here $C_k^m = \sqrt{\frac{4\pi}{2k+1}}Y_k^m$ are renormalized spherical harmonics, and $A_4^4 = A_4^{-4}$. The CEF parameters notation obtained can be found in Table I.

If one wishes to obtain the equivalent Stevens parameters [50], some care regarding the conversion from A_k^m needs to be taken, as multiple definitions can be found in literature. Here, we decided to solve the corresponding system that gives α, Δ_1, and Δ_2 as function of B_2^0, B_4^0, and B_4^4 below:

$$\begin{aligned}
&\arctan\left[\frac{(2\sqrt{5}B_4^4)}{\left(B_2^0 + 20B_4^0 - \sqrt{\left(B_2^0 + 20B_4^0\right)^2 + 20\left(B_4^4\right)^2}\right)}\right] \\
&= \sqrt{1-\alpha^2}; \\
&\quad -\frac{3}{2}\left(-8B_2^0 + 120B_4^0\right) - 6\sqrt{\left(B_2^0 + 20B_4^0\right)^2 + 20\left(B_4^4\right)^2} \\
&= -\Delta_2; \\
&\quad -\frac{3}{2}\left(-8B_2^0 + 120B_4^0\right) + 6\sqrt{\left(B_2^0 + 20B_4^0\right)^2 + 20\left(B_4^4\right)^2} \\
&= -(\Delta_2 - \Delta_1).
\end{aligned}$$

The corresponding Stevens parameters can be found in Table II.

TABLE II. Stevens CEF parameters (in K) obtained from XAS analysis, corresponding to the schemes in Fig. 2.

x	B_2^0	B_4^0	B_4^4
0	−5.90(1)	0.36(1)	−1.94(1)
0.5	−5.50(1)	0.34(1)	−2.69(1)
1	−4.88(1)	0.28(1)	−1.61(1)

APPENDIX B: METRIC FOR FIT QUALITY

In order to be able to verify the quality of our fit with a more quantitative metric, we calculate χ^2 for each temperature per composition and then proceed to calculate some statistic for this temperature-dependent χ^2 distribution,

$$\chi^2 = \sum_i \frac{(E_i - C_i)^2}{\sigma_i^2}. \tag{B1}$$

Here, to calculate χ^2 as defined by Eq. (B1), we need not only the ith experimental E_i and respective calculated C_i data point, but the associated experimental variance σ_i^2 of said point. To estimate the variance of the XAS spectra, whose instrumental component includes acquisition time, beam stability, precision of our Keithley electrometer and other smaller effects, we look at the pre-edge background noise of individual scans as an approximated measurement uncertainty. This allows us to calculate χ^2 for each experiment-simulation pair of curves per temperature per composition, as shown in Fig. 5(a). Then we calculate an average χ^2 per composition and its standard deviation, as shown in Fig. 5(b).

We observe in Fig. 5(a) that all fits present worse agreement around intermediate temperatures, which is intuitively expected since that is the energy range where the interplay of populations in each excited state is most sensitive. Further, Ce_2RhIn_8 displays worse overall agreement, while having

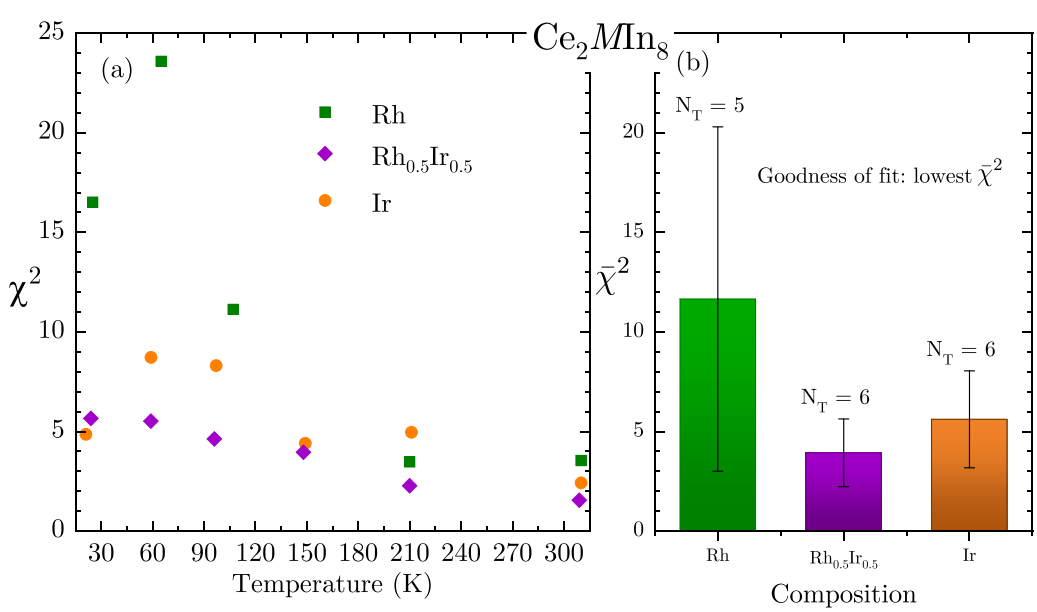

FIG. 5. (a) χ^2 calculated per temperature for each data-simulation pair of curves, for Ce_2RhIn_8 (squares), $Ce_2Rh_{0.5}Ir_{0.5}In_8$ (diamonds), and Ce_2IrIn_8 (circles). (b) Statistics over χ^2. The height of the bars represent the average χ^2 per compound, the error bars represent their standard deviation, and N_T is the number of temperatures considered per compound.

the least temperature points (namely five instead of six). Statistically we can understand this worse relative agreement since we have one less LD curve to use as a constraint to our model.

By averaging out the different $\chi^2(T)$, we not only get a numerical confirmation of those observations, but also we have some metric for the uncertainty of each fit. Given that the error bars in Fig. 5(b) are in a 3:1:2 ratio and the intrinsic uncertainty of the Δs in our full multiplet calculations are of about 1 meV, we increase the uncertainty of the energy splittings as to reproduce the goodness of fit we obtain.

[1] A. C. Hewson, *The Kondo Problem to Heavy Fermions* (Cambridge University Press, Cambridge, 1997), Vol. 2.

[2] J. Flouquet, in *On the Heavy Fermion Road*, edited by W. P. Halperin (Elsevier, Amsterdam, 2005), Vol. XV, pp. 139–268.

[3] P. Thalmeier and G. Zwicknagl, in *Handbook on the Phys. and Chem. of Rare Earths*, edited by J.-C. B. K. A. Gschneidner, Jr. and V. Pecharsky (Elsevier, Amsterdam, 2005), Vol. 34, pp. 139–268.

[4] P. Coleman, Heavy fermions: Electrons at the edge of magnetism, in *Handbook of Magn. and Adv. Magn. Mater.*, edited by M. F. S. M. H. Kronmüller, S. Parkin, and I. Zutic (John Wiley and Sons, Hoboken, NJ, 2007), Vol. 1, pp. 95–148.

[5] D. I. Khomskii, *Basic Aspects of the Quantum Theory of Solids: Order and Elementary Excitations* (Cambridge University Press, Cambridge, 2010).

[6] P. G. Pagliuso, N. J. Curro, N. O. Moreno, M. Hundley, J. D. Thompson, J. Sarrao, and Z. Fisk, Structurally tuned superconductivity in heavy-fermion $CeMIn_5$ (M= Co, Rh, Ir), Phys. B: Condens. Matter **320**, 370 (2002).

[7] A. D. Christianson, E. D. Bauer, J. M. Lawrence, P. S. Riseborough, N. O. Moreno, P. G. Pagliuso, J. L. Sarrao, J. D. Thompson, E. A. Goremychkin, F. R. Trouw, M. P. Hehlen, and R. J. McQueeney, Crystalline electric field effects in $CeMIn_5$ (M = Co, Rh, Ir): Superconductivity and the influence of kondo spin fluctuations, Phys. Rev. B **70**, 134505 (2004).

[8] P. Pagliuso, D. Garcia, E. Miranda, E. Granado, R. Lora Serrano, C. Giles, J. Duque, R. Urbano, C. Rettori, J. Thompson *et al.*, Evolution of the magnetic properties and magnetic structures along the R_mMIn_{3m+2} (R= Ce, Nd, Gd, Tb; M= Rh, Ir; and m= 1, 2) series of intermetallic compounds, J. Appl. Phys. **99**, 08P703 (2006).

[9] T. Willers, Z. Hu, N. Hollmann, P. O. Körner, J. Gegner, T. Burnus, H. Fujiwara, A. Tanaka, D. Schmitz, H. H. Hsieh, H.-J. Lin, C. T. Chen, E. D. Bauer, J. L. Sarrao, E. Goremychkin, M. Koza, L. H. Tjeng, and A. Severing, Crystal-field and Kondo-scale investigations of $CeMIn_5$ (m=Co, Ir, and Rh): A combined x-ray absorption and inelastic neutron scattering study, Phys. Rev. B **81**, 195114 (2010).

[10] T. Willers, F. Strigari, Z. Hu, V. Sessi, N. B. Brookes, E. D. Bauer, J. L. Sarrao, J. D. Thompson, A. Tanaka, S. Wirth, L. H. Tjeng, and A. Severing, Correlation between ground state and orbital anisotropy in heavy fermion materials, Proc. Natl. Acad. Sci. USA **112**, 2384 (2015).

[11] P. G. Pagliuso, J. D. Thompson, M. F. Hundley, J. L. Sarrao, and Z. Fisk, Crystal structure and low-temperature magnetic properties of R_mMIn_{3m+2} compounds (M= Rh or Ir; m= 1, 2; R= Sm or Gd), Phys. Rev. B **63**, 054426 (2001).

[12] J. D. Thompson, M. Nicklas, A. Bianchi, R. Movshovich, A. Llobet, W. Bao, A. Malinowski, M. F. Hundley, N. O. Moreno, P. G. Pagliuso *et al.*, Magnetism and unconventional superconductivity in $Ce_nM_mIn_{3n+2m}$ heavy-fermion crystals, Phys. B: Condens. Matter **329-333**, 446 (2003).

[13] E. Moshopoulou, Z. Fisk, J. Sarrao, and J. Thompson, Crystal growth and intergrowth structure of the new heavy fermion materials $CeIrIn_5$ and $CeRhIn_5$, J. Solid State Chem. **158**, 25 (2001).

[14] A. L. Cornelius, A. J. Arko, J. L. Sarrao, M. F. Hundley, and Z. Fisk, Anisotropic electronic and magnetic properties of the quasi-two-dimensional heavy-fermion antiferromagnet $CeRhIn_5$, Phys. Rev. B **62**, 14181 (2000).

[15] R. Settai, H. Shishido, S. Ikeda, Y. Murakawa, M. Nakashima, D. Aoki, Y. Haga, H. Harima, and Y. Onuki, Quasi-two-dimensional Fermi surfaces and the de Haas-van Alphen oscillation in both the normal and superconducting mixed states of $CeCoIn_5$, J. Phys.: Condens. Matter **13**, L627 (2001).

[16] Y. Haga, Y. Inada, H. Harima, K. Oikawa, M. Murakawa, H. Nakawaki, Y. Tokiwa, D. Aoki, H. Shishido, S. Ikeda, N. Watanabe, and Y. Onuki, Quasi-two-dimensional Fermi surfaces of the heavy Fermion superconductor $CeIrIn_5$, Phys. Rev. B **63**, 060503(R) (2001).

[17] H. C. Choi, B. I. Min, J. H. Shim, K. Haule, and G. Kotliar, Temperature-dependent Fermi surface evolution in heavy fermion $CeIrIn_5$, Phys. Rev. Lett. **108**, 016402 (2012).

[18] L. Jiao, Y. Chen, Y. Kohama, D. Graf, E. Bauer, J. Singleton, J.-X. Zhu, Z. Weng, G. Pang, T. Shang *et al.*, Anisotropic electronic and magnetic properties of the quasi-two-dimensional heavy-fermion antiferromagnet $CeRhIn_5$, Proc. Natl. Acad. Sci. USA **112**, 673 (2015).

[19] E. N. Hering, H. A. Borges, S. M. Ramos, M. B. Fontes, E. Baggio-Saitovich, M. A. Continentino, E. M. Bittar, L. Mendonca Ferreira, R. Lora-Serrano, F. C. G. Gandra, C. Adriano, P. G. Pagliuso, N. O. Moreno, J. L. Sarrao, and J. D. Thompson, Residual superconducting phases in the disordered $Ce_2Rh_{1-x}Ir_xIn_8$ alloys, Phys. Rev. B **82**, 184517 (2010).

[20] G. D. Morris, R. H. Heffner, N. O. Moreno, P. G. Pagliuso, J. L. Sarrao, S. R. Dunsiger, G. J. Nieuwenhuys, D. E. MacLaughlin, and O. O. Bernal, Random spin freezing in Ce_2MIn_8 (M= Co, Rh, Ir) heavy-fermion materials, Phys. Rev. B **69**, 214415 (2004).

[21] N. Moreno, M. Hundley, P. Pagliuso, R. Movshovich, M. Nicklas, J. Thompson, J. Sarrao, and Z. Fisk, Physical properties of $Ce_2(Rh, Ir)_{1-x}Co_xIn_8$, Phys. B: Condens. Matter **312-313**, 274 (2002).

[22] J. D. Thompson and Z. Fisk, Progress in heavy-fermion superconductivity: Ce115 and related materials, J. Phys. Soc. Jpn. **81**, 011002 (2012).

[23] G. Chen, S. Ohara, M. Hedo, Y. Uwatoko, K. Saito, M. Sorai, and I. Sakamoto, Observation of superconductivity in heavy-fermion compounds of Ce_2CoIn_8, J. Phys. Soc. Jpn. **71**, 2836 (2002).

[24] R. T. Macaluso, J. Sarrao, N. Moreno, P. Pagliuso, J. Thompson, F. R. Fronczek, M. Hundley, A. Malinowski, and J. Y. Chan, Single-crystal growth of Ln_2MIn_8 (Ln= La, Ce; M= Rh, Ir): Implications for the heavy-fermion ground state, Chem. Mater. **15**, 1394 (2003).

[25] E. Moshopoulou, R. Ibberson, J. Sarrao, J. Thompson, and Z. Fisk, Structure of Ce_2RhIn_8: An example of complementary use of high-resolution neutron powder diffraction and reciprocal-space mapping to study complex materials, Acta Cryst. B **62**, 173 (2006).

[26] D. S. Christovam, M. Ferreira-Carvalho, A. Marino, M. Sundermann, D. Takegami, A. Melendez-Sans, K. D. Tsuei, Z. Hu, S. Rößler, M. Valvidares *et al.*, Spectroscopic evidence of Kondo-induced quasiquartet in $CeRh_2As_2$, Phys. Rev. Lett. **132**, 046401 (2024).

[27] D. S. Christovam, C. Giles, L. Mendonça-Ferreira, J. Leao, W. Ratcliff, J. W. Lynn, S. Ramos, E. N. Hering, H. Hidaka, E. Baggio-Saitovich, Z. Fisk, P.G. Pagliuso, and C. Adriano, Spin rotation induced by applied pressure in the Cd-doped Ce_2RhIn_8 intermetallic compound, Phys. Rev. B **100**, 165133 (2019).

[28] D. S. Christovam, G. S. Freitas, M. M. Piva, J. C. Souza, M. O. Malcolms, O. L. Canton, J. B. Leão, W. Ratcliff, J. W. Lynn, C. Adriano, and P. G. Pagliuso, Evolution of the magnetic properties in the antiferromagnet Ce_2RhIn_8 simultaneously doped with Cd and Ir, Phys. Rev. B **102**, 195137 (2020).

[29] P. Hansmann, A. Severing, Z. Hu, M. W. Haverkort, C. F. Chang, S. Klein, A. Tanaka, H. H. Hsieh, H.-J. Lin, C. T. Chen, B. Fåk, P. Lejay, and L. H. Tjeng, Determining the crystal-field ground state in rare earth heavy fermion materials using soft-X-ray absorption spectroscopy, Phys. Rev. Lett. **100**, 066405 (2008).

[30] T. Willers, D. T. Adroja, B. D. Rainford, Z. Hu, N. Hollmann, P. O. Körner, Y.-Y. Chin, D. Schmitz, H. H. Hsieh, H.-J. Lin, C. T. Chen, E. D. Bauer, J. L. Sarrao, K. J. McClellan, D. Byler, C. Geibel, F. Steglich, H. Aoki, P. Lejay, A. Tanaka, L. H. Tjeng, and A. Severing, Spectroscopic determination of crystal-field levels in $CeRh_2Si_2$ and $CeRu_2Si_2$ and of the $4f^0$ contributions in CeM_2Si_2 (M = Cu, Ru, Rh, Pd, and Au), Phys. Rev. B **85**, 035117 (2012).

[31] M. Sundermann, A. Amorese, F. Strigari, B. Leedahl, L. H. Tjeng, M. W. Haverkort, H. Gretarsson, H. Yavaş, M. M. Sala, E. D. Bauer, P. F. S. Rosa, J. D. Thompson, and A. Severing, Orientation of the ground-state orbital in $CeCoIn_5$ and $CeRhIn_5$, Phys. Rev. B **99**, 235143 (2019).

[32] Z. Fisk and J. P. Remeika, *Handbook on the Physics and Chemistry of Rare Earths* (Elsevier, North-Holland, 1989).

[33] M. Binnewies, J. Dolinšek, F. Failamani, M. Feuerbacher, Z. Fisk, G. Guélou, Q. Guo, M. Hedo, Z. Henkie, H. Ipser *et al.*, *Crystal Growth of Intermetallics* (Walter de Gruyter, Berlin, 2018).

[34] H.-M. Tsai, H.-W. Fu, C.-Y. Kuo, L.-J. Huang, C.-S. Lee, C.-Y. Hua, K.-Y. Kao, H.-J. Lin, H.-S. Fung, S.-C. Chung *et al.*, A submicron soft x-ray active grating monochromator beamline for ultra-high resolution angle-resolved photoemission spectroscopy, in *AIP Conference Proceedings*, Vol. 2054 (AIP Publishing, Melville, NY, 2019).

[35] M. W. Haverkort, *Quanty* for core level spectroscopy - excitons, resonances and band excitations in time and frequency domain, J. Phys.: Conf. Ser. **712**, 012001 (2016).

[36] R. Cowan, *The Theory of Atomic Structure and Spectra* (University of California, Berkeley, 1981).

[37] A. Tanaka and T. Jo, Resonant 3d, 3p and 3s photoemission in transition metal oxides predicted at 2p threshold, J. Phys. Soc. Jpn. **63**, 2788 (1994).

[38] B. G. Jang, B. Goh, J. Kim, J. N. Kim, H. Kang, K. Haule, G. Kotliar, H. Choi, and J. H. Shim, Orbital anisotropy of heavy fermion Ce_2IrIn_8 under crystalline electric field and its energy scale, Phys. Rev. B **105**, 115147 (2022).

[39] A. Malinowski, M. F. Hundley, N. O. Moreno, P. G. Pagliuso, J. L. Sarrao, and J. D. Thompson, Thermal expansion and magnetovolume effects in the heavy-fermion system Ce_2RhIn_8, Phys. Rev. B **68**, 184419 (2003).

[40] F. de Groot and A. Kotani, *Core Level Spectroscopy of Solids* (CRC Press, Amsterdam, 2008).

[41] O. Gunnarsson, K. Schönhammer, J. Allen, K. Karlsson, and O. Jepsen, Information from photoemission spectral weights and shapes, J. Electron Spectrosc. Relat. Phenom. **117-118**, 1 (2001).

[42] F. Strigari, M. Sundermann, Y. Muro, K. Yutani, T. Takabatake, K.-D. Tsuei, Y. Liao, A. Tanaka, P. Thalmeier, M. Haverkort *et al.*, Quantitative study of valence and configuration interaction parameters of the kondo semiconductors CeM_2Al_{10} (M= Ru, Os and Fe) by means of bulk-sensitive hard X-ray photoelectron spectroscopy, J. Electron Spectrosc. Relat. Phenom. **199**, 56 (2015).

[43] P. Boutron, Exact calculation of the paramagnetic susceptibility of a single crystal with arbitrary crystal field and exchange interactions, Phys. Rev. B **7**, 3226 (1973).

[44] W. Bao, P. G. Pagliuso, J. L. Sarrao, J. D. Thompson, Z. Fisk, and J. W. Lynn, Magnetic structure of heavy-fermion Ce_2RhIn_8, Phys. Rev. B **64**, 020401(R) (2001).

[45] K. Chen, F. Strigari, M. Sundermann, Z. Hu, Z. Fisk, E. D. Bauer, P. F. S. Rosa, J. L. Sarrao, J. D. Thompson, J. Herrero-Martin *et al.*, Evolution of ground-state wave function in $CeCoIn_5$ upon Cd or Sn doping, Phys. Rev. B **97**, 045134 (2018).

[46] M. Nicklas, V. A. Sidorov, H. A. Borges, P. G. Pagliuso, J. L. Sarrao, and J. D. Thompson, Two superconducting phases in $CeRh_{1-x}Ir_xIn_5$, Phys. Rev. B **70**, 020505(R) (2004).

[47] I. Sakamoto, Y. Shomi, and S. Ohara, Anomalous hall effect in heavy fermion compounds Ce_2MIn_8 (M= Rh, Ir), Phys. B: Condens. Matter **329-333**, 607 (2003).

[48] C. Petrovic, P. G. Pagliuso, M. F. Hundley, R. Movshovich, J. L. Sarrao, J. D. Thompson, Z. Fisk, and P. Monthoux, Heavy-fermion superconductivity in $CeCoin_5$ at 2.3 k, J. Phys.: Condens. Matter **13**, L337 (2001).

[49] S. Süllow, A. Otop, A. Loose, J. Klenke, O. Prokhnenko, R. Feyerherm, R. WA Hendrikx, J. A. Mydosh, and H. Amitsuka, Electronic localization and two-dimensional metallic state in UPt_2Si_2, J. Phys. Soc. Jpn. **77**, 024708 (2008).

[50] K. Stevens, Matrix elements and operator equivalents connected with the magnetic properties of rare earth ions, Proc. Phys. Soc. Sect. A **65**, 209 (1952).